

# Structural Characterization of the Taltal Segment in Northern Chile Between 22°S and 26°S Using Local Earthquake Tomography

Sergio Leon-Rios<sup>1</sup>, Valentina Reyes-Wagner<sup>1</sup>, Daniela Calle-Gardella<sup>1</sup>, Andrei Maksymowicz<sup>2</sup>, Andreas Rietbrock<sup>3</sup>, Steven Roecker<sup>4</sup>, and Diana Comte<sup>1,2</sup>

<sup>1</sup>Advanced Mining Technology Center, Universidad de Chile

<sup>2</sup>Departamento de Geofísica, Universidad de Chile

<sup>3</sup>Geophysical Institute, Karlsruhe Institute of Technology

<sup>4</sup>Rensselaer Polytechnic Institute

September 25, 2023

1 **Structural Characterization of the Taltal Segment in Northern Chile Between**  
2 **22°S and 26°S Using Local Earthquake Tomography**

3

4 Sergio Leon-Rios<sup>1</sup>, Valentina Reyes-Wagner<sup>1</sup>, Daniela Calle-Gardella<sup>1</sup>, Andreas Rietbrock<sup>2</sup>,  
5 Steven Roecker<sup>3</sup>, Andrei Maksymowicz<sup>4</sup> and Diana Comte<sup>1,4</sup>

6 <sup>1</sup> Advanced Mining Technology Center, Facultad de Ciencias Físicas y Matemáticas,  
7 Universidad de Chile. Chile.

8 <sup>2</sup> Geophysical Institute, Karlsruhe Institute of Technology, Germany.

9 <sup>3</sup> Earth and Environmental Sciences, Rensselaer Polytechnic Institute, USA.

10 <sup>4</sup> Departamento de Geofísica, Facultad de Ciencias Físicas y Matemáticas, Universidad de  
11 Chile. Chile.

12

13 **Keypoints**

14 - Seismic catalog reveals forearc activity and slab dip variations. Vp anomalies in  
15 oceanic plate are associated with mid-depth seismic events. The seismic catalog  
16 revealed active structures in the forearc, dip changes along the slab and fracturing  
17 in the Nazca & South American plates

18

19 - Vp/Vs model uncovers oceanic and continental plate anomalies that influence  
20 seismicity, including fault systems and hydration changes

21

22 - Shallow low Vp/Vs (<1.75) correlate with ore deposits; deep high Vp/Vs (>1.80)  
23 suggest fluids and melting for the Lastarria volcanic complex

24

25

26

27 **Abstract**

28 Recordings of earthquakes by a temporary deployment of 88 short period seismometers  
29 in northern Chile were used to derive regional 3D seismic velocity models for the Taltal  
30 segment. We used the Regressive ESTimator (REST) package for event detection and  
31 automatic onset estimation of P- and S-wave arrival times to create an earthquake catalog  
32 with 23,985 hypocenters. We followed standard acceptability criteria to create a high-  
33 quality dataset and inverted for 3D  $V_p$ ,  $V_s$  and  $V_p/V_s$  models using local earthquake  
34 tomography.

35 Plots of hypocenters from the catalog reveal active structures in the upper crust, dip  
36 changes along the slab and fracturing within the oceanic crust. The wavespeed models  
37 illuminated several features in both the Nazca and South American plate, including the  
38 Atacama fault system on the coastline and the Domeyko Fault System in the forearc.  
39 These models also provide evidence for fluid circulation caused by the subducting Taltal  
40 ridge on the coast and partial melting feeding a volcanic complex close to the Andes.  
41 Anomalously low  $V_p/V_s$  ratios ( $<1.77$ ) are associated with copper mining operations in the  
42 area, suggesting that this kind of imaging can be used to characterize the distribution of  
43 ore deposits in the area.

44

45 **Plain language summary**

46 We recorded earthquakes in northern Chile with a network of 88 seismometers and used  
47 the arrival times of P and S waves to generate 3D wavespeed models of the region. These  
48 models reveal several structures in the area, including changes in the angle of the  
49 subducting Nazca plate and fractures in the oceanic crust. Among features observed in  
50 both the Nazca and South American plates are the Atacama and Domeyko fault systems.  
51 We also infer fluid circulation caused by the subducting Taltal ridge and partial melting  
52 that is feeding a volcanic complex near the Andes. Low values of the  $V_p/V_s$  ratio are  
53 associated with copper mining operations in the area and could be used to identify new  
54 ore deposits.

55 **Keywords:** Northern Chile, 3D Velocity Models, Tectonic Processes, Local Earthquake  
56 Tomography, Seismic Catalog, Continental Forearc

57

## 58 **1. Introduction**

59 The geologically active margin in northern Chile, where the oceanic Nazca plate subducts  
60 beneath the continental South American plate at a relative rate of  $\sim 6.0\text{-}7.0$  mm/yr  
61 (DeMets et al., 1990, 1994; Angermann et al., 1999; Norabuena et al., 1999; Sella et al.,  
62 2002) offers an ideal setting for seismic investigations of the subduction process in  
63 tectonically erosive margins. The lack of anthropogenic noise and the dryness of the soil  
64 allow for high SNR recordings of seismic signals. A variety of heterogeneities, such as  
65 seamounts and ridges on the oceanic crust, along with the prominent peninsulas along the  
66 coast, contribute to diverse modes by which stress in the region is accumulated and  
67 released. In particular, a number of studies have focused on the large thrust events in the  
68 area, such as the M8.0 Antofagasta earthquake in 1995 (Monfret et al., 1995; Ruegg et al.,  
69 1996; Delouis et al., 1997), the M7.8 Tocopilla earthquake in 2007 (Delouis et al., 2009;  
70 Peyrat et al., 2010; Bejar-Pizarro et al., 2010), and a proposed  $M_w \sim 9.5$  earthquake  
71 (Salazar et al., 2022) 3800 years ago in the Taltal segment between  $22^\circ\text{S}$  and  $26^\circ\text{S}$  (Figure  
72 1). In the same area, long-term geodetic studies have quantified the degree of seismic  
73 coupling (Chlieh et al., 2004; Metois et al., 2013; Metois et al., 2016; Klein et al., 2018) and  
74 the capacity of the area to host a large megathrust earthquake (Yañez-Cuadra et al.,  
75 2022). Several recent investigations have focused on understanding the sources of  
76 seismicity in northern Chile. For example, Mavor et al. (2020) described the kinematics  
77 and tectonic evolution of the Taltal Fault, Sippl et al. (2023) used a 15-year seismic catalog  
78 to summarize the activity in northern Chile, and Gonzalez-Vidal (personal communication,  
79 2023) deployed a temporary network to explore the relations between heterogeneity in  
80 the subducting plate and the degree of interplate locking. In terms of seismic imaging of  
81 this zone, Husen et al. (2000), together with Haberland and Rietbrock (2001), set  
82 foundations for tomographic analysis by deriving seismic velocity and attenuation models,

83 respectively. However, despite all these studies, the tectonic processes at a regional scale  
84 - from the coastline to the volcanic arc - have been largely ignored.

85 To investigate the roles that features such as a subducting ridge and crustal faults play in  
86 the overall tectonics and in the high intermediate-depth seismicity rate of the Taltal  
87 segment, we analyzed data from a passive seismic experiment comprising a large network  
88 of seismic sensors. The size and the density of this temporary deployment along with the  
89 high rate of seismicity in this area (e.g., CSN technical report for the seismicity in Chile  
90 2018, 2019, 2020; [www.csn.uchile.cl](http://www.csn.uchile.cl)) facilitates applications of high-resolution imaging  
91 using local earthquake tomography (LET). This method uses the arrival times of P- and S-  
92 phases generated by local earthquakes to derive 3D seismic velocity models for  $V_p$ ,  $V_s$  and  
93  $V_p/V_s$  that highlight the structures and anomalies in the subsurface (e.g., Aki and Lee,  
94 1976; Eberhart-Phillips et al., 1986; Thurber et al., 1995). In this study, we apply this type  
95 of analysis to investigate the distribution of fluids in the Taltal segment and its potential  
96 relation to the seismic activity between and within the oceanic and the continental, plates  
97 (e.g., Christensen, 1996; Moreno et al., 2012; Contreras-Reyes et al., 2021). The large  
98 amount of seismic data recorded by this deployment allows us to image the main  
99 geological structures and areas of fluid circulation that control the seismic activity at  
100 shallow- (<30 km) and intermediate-depth (~100-200 km) in the segment.

101

## 102 **2. Tectonic setting**

103 During the past century, only moderate magnitude earthquakes (7.5-8.5) have been  
104 documented in the Taltal segment (Figure 1). These include the intraplate M8.0 Calama  
105 earthquake in 1950 (Kausel & Campos, 1992), the M7.7 and M7.6 Taltal earthquakes in  
106 1966 (Deschamps, 1980) and 1987 (Ruiz and Madariaga, 2018), the interplate M8.1  
107 Antofagasta earthquake in 1995 (Monfret et al., 1995; Ruegg et al., 1996; Delouis et al.,  
108 1997) and the interplate M7.7 Tocopilla earthquake in 2007 (Delouis et al., 2009; Bejar-  
109 Pizarro et al., 2010; Peyrat et al., 2010); all of them located in the northern part of the  
110 segment (22°S-25°S). Only one documented megathrust earthquake struck the southern

111 part of this region in 1922 ( $M \sim 8.5$ , Willis 1929; Abe 1979; Beck, 1998; Comte et al., 2002b;  
112 Kanamori et al., 2019), which, due the absence of megathrust events with  $M > 8.5$  in the  
113 past (Ruiz and Madariaga, 2018) has led to some authors to refer to this portion of the  
114 segment ( $25^\circ\text{S}$ - $27^\circ\text{S}$ ) as atypical for the Chilean margin. At the same time, the  
115 multidisciplinary study of Salazar et al. (2022) inferred that, based on the effects on  
116 ancient inhabitants, a large earthquake and tsunami occurred  $\sim 3800$  yrs ago, suggesting  
117 that the area it is capable of hosting large megathrust earthquakes similar to the 2010  
118 Maule and 1960 Valdivia event in other regions of Chile (e.g., Kelleher, 1972; Ruiz &  
119 Madariaga, 2018). While megathrusts are infrequent, swarms of seismicity are common in  
120 this area (Comte et al., 2002a; Holtkamp et al., 2011; Metois et al., 2016) suggesting that  
121 heterogeneities along the plate interface complicate this portion of the Taltal segment.

122 Offshore, irregularities in the bathymetry of the seafloor such as the Mejillones Fracture  
123 Zone (MFZ, Maksymowicz 2015) and the Taltal ridge (Figure 1a) have been proposed to  
124 cause a seismogenic segmentation in the region that stops the rupture propagation of  
125 local megathrust earthquakes (Maksymowicz, 2015). Pasten-Araya et al. (2021) discussed  
126 the presence of a splay fault close to the coastline in the region and emphasized the  
127 importance of these types of structures for seismic hazards. Onshore (Figure 1a), the  
128 region has two main N-S fault systems, the Atacama fault system (AFS) and Domeyko fault  
129 system (DFS), that were formed in response to an oblique transfer of subduction stress  
130 (Mavor et al., 2020 and reference therein). The upper-crust is further complicated by  
131 several other small geological structures with diverse lineaments and length, such as the  
132 Mejillones fault (MF), the Taltal fault (TTF), the Calama-Olacapato-El Toro lineament (COT)  
133 and others (Figure 1a; Arabasz 1968; Arabasz Jr, 1971). These lithospheric scale features  
134 should play a critical role in the behavior of crustal seismicity and in the distribution of  
135 abundant porphyry copper deposits (Cooke et al., 2005; Richards, 2016).

136 The volcanic arc in this area is shifted towards the east relative to its position to the north  
137 and south (Figure 1a), which has been explained by a region of high-density located below  
138 the Salar de Atacama (Götze and Krause, 2002; Schurr and Rietbrock, 2004). Eastward, an  
139 analysis of electrical resistivity (Diaz et al., 2012; Pritchard et al., 2018; Kühn et al., 2018;

140 Araya-Vargas et al., 2019) and receiver function studies (Ward et al., 2017; Delph et al.,  
141 2017) show two large magmatic bodies, the Altiplano-Puna (APMB) and Lazufre (LMB), are  
142 located at the edges of the area of interest, with smaller magmatic bodies in between.

143

### 144 **3. Data and Methods**

#### 145 *Dataset: The Taltal seismic experiment*

146 The data analyzed in this study were recorded by a temporary network deployed as part  
147 of a joint effort between the Advanced Mining Technology Center (AMTC) of Universidad  
148 de Chile and the Geophysical Institute from the Karlsruhe Institute of Technology (KIT) of  
149 Germany and comprised 84 triaxial short period geophones (3D Geophone HL-6B, 4.5 Hz)  
150 and Datacube<sup>3</sup> digitizers sampling at 200 Hz. The instruments covered an area of ~127,000  
151 km<sup>2</sup> and operated between March and October 2020 (Figure 1b).

#### 152 *Seismic catalog and onset detection*

153 The seismic traces recorded by the Taltal experiment were processed using the Regressive  
154 ESTimator (REST) automatic picking package described in Comte et al. (2019). REST uses  
155 the autoregressive approach of Pisarenko et al. (1987) and Kushnir et al. (1990), combined  
156 with data windowing procedures suggested by Rawles and Thurber (2015), to generate  
157 detections and onset estimates of phase arrivals. The functions used for detection and  
158 onset estimation are indifferent to waveform morphology, relying instead on statistical  
159 estimates of similarity and predictability between a subset of samples and a  
160 representation of background noise. Hypocenters are determined using a grid search  
161 location scheme (Roecker et al., 2004; 2006) with travel times calculated in a wavespeed  
162 model specified at a 3D distribution of nodes in a spherical coordinate system.

163 In this study, we adopted a reference 1D velocity model based on the results of Husen et  
164 al. (1999) for shallow and intermediate depths (0-50 km) and IASP91 (Kenneth & Engdahl,  
165 1991) for depths > 50 km. Wavespeeds and travel times are specified on a 3D grid of  
166 157,500 nodes separated by 10 km over an area of 700 x 750 km<sup>2</sup> and 285 km depth.

167 Events included in the inversion were required to have a minimum of 10 phases and an  
168 arrival time residual of less than 2.0 s, resulting in an initial catalog of 23,985 earthquakes  
169 with 774,989 P- and 667,114 S-wave arrival times with an overall root mean square (RMS)  
170 residual of 0.48 s. In carrying out the LET, we further refine the catalog by applying a  
171 stricter selection criterion requiring (1) an azimuthal gap in recording stations of less than  
172 210°, (2) a minimum of 20 total phases, and (3) a maximum residual of 1.5 s. The refined  
173 catalog contains 12,851 earthquakes with 415,425 P and 358,770 S arrival times.

#### 174 *Three-dimensional seismic velocity models*

175 The arrival times in the refined catalog were used to generate a 3D velocity model for Vp  
176 and Vp/Vs using the joint inversion methodology described in Roecker et al. (2004, 2006).  
177 The algorithm parametrizes the subsurface as a volumetric grid in a spherical coordinate  
178 system and performs an iterative process that jointly inverts for earthquake locations, Vp,  
179 and either Vs or Vp/Vs. The process stops after the reduction in the residual variance  
180 becomes statistically insignificant.

181 The grid has 677,376 nodes spaced at 5 km and covers an area of 540 x 560 km<sup>2</sup> and from  
182 the surface to a depth of 270 km. The initial Vp model is the same 1D model used to  
183 generate the catalog, and an initial Vp/Vs of 1.77 estimated from a Wadati diagram  
184 (Wadati et al., 1933; Kisslinger and Engdahl, 1973; Supporting Information 2) of P and S  
185 arrival times. An optimal damping factor is estimated using trade-off curves (Supporting  
186 Information 1) of residual and model variance, the latter being defined using the  
187 “roughness” parameter of Greenfield et al. (2016). The preferred model is obtained after  
188 16 iterations showing an overall RMS of 0.25 s and a variance of 0.15 s. and residuals (see  
189 Supporting Information 3). These values represent a decrease of about 37% in RMS and  
190 45% in variance compared to those from the initial model. Final hypocenters have average  
191 arrival time residuals of 0.13 s and 0.79 s for P- and S-wave onsets, respectively. Location  
192 uncertainties estimated from marginal probability density functions are on the order of 6  
193 km, 5 km, and 8 km for the east, north and depth coordinates, respectively.

194

195 *Model Resolution*

196 Based on the results of numerous previous LET investigations, the distribution of events  
197 and stations in this study would lead one to expect an overall spatial resolution of  
198 structure on the order of tens of km. Nevertheless, the irregular distribution of both  
199 stations and earthquakes and the highly nonlinear nature of the inverse problem requires  
200 that we document how resolution varies within the model volume. Two common ways to  
201 assess the resolution of seismic velocity models are the checkerboard test (e.g., Spakman  
202 and Nolet, 1988) and bootstrap resampling (e.g., Calvert et al., 2000; Hicks et al., 2014;  
203 León-Ríos et al., 2021). In both cases, synthetic data are calculated in hypothetical models  
204 with different sizes and shapes of velocity anomalies. Random noise based on the  
205 standard deviation is typically added to the synthetic data to simulate actual data quality  
206 (e.g., Hicks et al., 2014; Comte et al., 2019). These synthetic datasets are then inverted  
207 following the same procedure as that for the real data and a comparison between the  
208 actual and recovered models is made to evaluate resolution scale lengths.

209 *Checkerboard test*

210 The checkerboard resolution tests assumed equi-dimensional anomalies of 15 km, 20 km  
211 and 30 km length scale, within which velocities were perturbed by  $\pm 5\%$  to form a  
212 checkerboard pattern (Supporting Information 4 and 5). Gaussian noise of  $1/3 \sigma$  of arrival  
213 time was added to the synthetic data at a level commensurate with the anticipated  
214 uncertainties in the observations, and the result was inverted following the same  
215 procedure as that for the actual model. The results for the 15 km dimension anomaly  
216 (Supporting Information 4 and 5) show that it is possible to recover the initial  
217 perturbations in much of the model volume at this scale. In general, we infer that the  
218 data is capable of recovering wavespeed variations at this scale down to 150 km with a  
219 geometry consistent with the shape of the subduction margin. Tests performed with  
220 smaller dimension perturbations indicate that 15 km anomalies are the smallest size for  
221 interpreting possible geological structures.

222

### 223 *Bootstrap resampling*

224 The bootstrapping technique is useful to assess the sensitivity of seismic velocity models  
225 with respect to the completeness of the event catalog. The bootstrap resampling method  
226 suggests that event-based resampling should produce similar results to resampling  
227 individual picks (e.g., Calvert et al., 2000; Hicks et al., 2014). We randomly selected 80% of  
228 the events in the original data and inverted following the same procedure as for the actual  
229 models. Resulting Vp, Vs and Vp/Vs seismic velocity models (see Supporting Information  
230 6) recover most of the anomalies observed in the actual models indicating that the results  
231 are insensitive to the event selection criteria. Uncertainties estimated from the  
232 bootstrapped resampling are about  $\pm 0.025$  km/s for Vp and Vs and about  $\pm 0.004$  for  
233 Vp/Vs.

234

## 235 **4. Results**

### 236 *Hypocenter catalog*

237 The catalog of well constrained locations has 16,349 events with an average location  
238 uncertainty of 6.90 km. Most of the events with depths between 30 km to 120 km depth  
239 are located along the subduction interface (slab 2.0, Hayes et al., 2018; Figure 2). Shallow  
240 seismicity (<10 km) is associated with the location of mining operations (Figure 2).  
241 Earthquakes in the northern part of the model (cross sections P1-P4) are predominantly  
242 intermediate-depth (80 km - 120 km depth), while those in the south (cross-sections P5-  
243 P8) are more evenly distributed along the plate interface. The northernmost sections (P1  
244 and P2) include upper crustal seismicity that correlates spatially with both the Atacama  
245 and Domeyko fault systems, consistent with the active nature of these large-scale systems  
246 (Comte et al., 2002b; Bloch et al., 2014; Sippl et al., 2018; 2023). Section P2 also shows a  
247 cluster of seismicity at the coast located within the Nazca plate at  $\sim 40$  km depth that is  
248 consistent with the Michilla cluster identified in previous catalogues from Fuenzalida et al.  
249 (2013) and Pasten-Araya et al. (2021) after the 2007 Tocopilla earthquake. At greater  
250 depths ( $\sim 80 - 110$  km), clusters of seismicity (C1 in Figure 2) are found within the Nazca

251 plate. An additional dense cluster of seismicity evident in section P4 (Figure 2)  
252 corresponds to the Jujuy seismic nest (Valenzuela-Malebran et al. 2022). We observe  
253 seismicity at shallower depths (<50 km) in section P5 at a distance of ~400 km from the  
254 trench that might be related to volcanic activity from either the Lazufre magmatic body or  
255 the Altiplano-Puna magmatic body (Ward et al., 2014; 2017). Sections P6 and P7 show  
256 offshore clustered seismicity with an NNW trend and a west dipping alignment that  
257 reaches down to the plate interface which is consistent with the observations from  
258 Gonzalez-Vidal et al. (2023). Similar NNW seismicity lineaments are observed to the north  
259 (from profile P4 to P6, Figure 2), which suggests a regional structural pattern in this  
260 segment of the margin. In fact, these kinds of seismicity lineaments were previously  
261 observed further north by Pasten-Araya et al. (2021), who identified an active offshore  
262 splay fault off the coast of Antofagasta. The observed shallow seismicity in profiles P4-P7  
263 suggests a similar active structure to the south of 24°S.

264

#### 265 *Seismic tomography*

266 First order structures observed in the tomographic models (Figure 3, 4, S7 and S8) include  
267 the Nazca plate imaged to depths of ~100 km with an east dipping anomaly with  $V_p \sim 7.0 -$   
268  $8.0$  km/s and  $V_s \sim 4.0 - 4.5$  km/s. The South American plate shows  $V_p$  values of  $\sim 5.0 - 7.0$   
269 km/s and  $V_s \sim 3.0 - 4.0$  km/s which are consistent with those found in previous  
270 investigations (Husen et al., 2000; Haberland and Rietbrock, 2001; Schurr et al., 2006;  
271 Pasten-Araya et al., 2021). The average value of  $V_p/V_s$  determined with the Wadati  
272 diagram (Wadati et al., 1933;  $V_p/V_s = 1.77$ ) is retained in the inversion. We observe a  
273 heterogeneous distribution of anomalies in the whole segment with several transition  
274 areas from high ( $V_p/V_s > 1.80$ ) to low ( $V_p/V_s < 1.80$ ) ratios observed in both lower and  
275 upper plate (Figure 3 and 4). These anomalies and transition areas can be correlated with  
276 geological structures observed at the surface, such as the AFS, DFS, the Salar de Atacama,  
277 and the Salar Punta Negra (see section  $z = 10$  km in Figure 4).

278 In a closer view of the continental crust, section P1 (Figure 3) shows a heterogeneous  
279 velocity structure with  $V_p \sim 6.0$  km/s in the first 10 km depth and between 6.0 -7.0 km/s at  
280 10 – 30 km depth. The  $V_p/V_s$  model shows an anomaly ( $>1.80$ ; labeled A1 in Figure 4)  
281 located at the coastline in the upper crust. Eastward, the model shows a low  $V_p/V_s$  patch  
282 ( $<1.74$ ; labeled A2 in Figure 4), that extends along the whole segment at  $\sim 69^\circ\text{W}$  from near  
283 the surface to 30 km depth (Figure 4). In section P2 the upper crust shows a more  
284 heterogeneous forearc between 200 – 300 km from the trench with  $V_p \sim 6.5$  down to 30  
285 km depth and alternating patches with low and high  $V_p/V_s$  regions. In particular, the  
286  $V_p/V_s$  model illuminates a large high ratio ( $>1.82$ ) anomaly located at shallow depths  
287 which is coincident with the location of the Salar de Atacama. The model also shows  
288 transitions from high ( $>1.80$ ) to low ( $<1.75$ )  $V_p/V_s$  ratios highlighting the heterogeneity of  
289 the segment across the forearc. Continuing to the south, sections P3 to P6 for  $V_p/V_s$  show  
290 two large patches (A2, A5) with low ratios ( $<1.75$ ) which are contoured by sub-vertical  
291 elongated anomalies ( $V_p/V_s > 1.77$ ) that reach down to the interplate interface. Another  
292 unusual vertical-elongated feature appears at  $24^\circ\text{-}24.5^\circ\text{S}$ , in section P4 and P5, below the  
293 Cordillera de los Andes. This anomaly (A6), with  $V_p/V_s \sim 1.80$ , is accompanied by shallow  
294 seismicity and is coincident with a low resistivity feature identified by other geophysical  
295 studies in the area (Diaz et al., 2012; Araya-Vargas et al., 2019).

296 In the region of the mantle wedge, interplate boundary and subducted plate, P1 shows an  
297 area of  $V_p \sim 8.0$  km/s close to the plate interface at 50 km depth that locates above a  
298 cluster of seismicity within the Nazca plate. At greater depths ( $>80 - 100$  km), we observe  
299 a large (150 km width x 40 km depth) low  $V_p/V_s$  ( $<1.80$ ; labeled A3 in Figure 4) which  
300 correlates with the clustered seismicity within the oceanic crust. In section P2, the 8.0  
301 km/s  $V_p$  east-dipping-contour shifts upwards in comparison to P1. In this section, at  
302 distances  $>300$  km from the trench and at  $\sim 50\text{-}70$  km depth, we find areas with  $V_p$  values  
303  $> 7.6\text{-}7.8$  km/s that illuminate the mantle wedge that are consistent with values suggested  
304 by Comte et al. (2023). In sections P3 to P6,  $V_p$  in the lower part of the oceanic plate has a  
305 value of 8.2 km/s (labeled A4 in Figure 4). The oceanic slab here has  $V_p/V_s$  ratios  $> 1.82$ ,  
306 distinguishing it from the slab in the northern profiles. Sections P6, P7 and P8 show a

307 westward shift of the mantle wedge marked by the  $V_p \sim 7.6-7.8$  km/s contours at a  
308 distance about 300 km from the trench.  $V_p/V_s$  in the vicinity of the Taltal ridge in sections  
309 P6 and P7 (labeled A7 in Figure 4) is low ( $<1.76$ ). A similar feature, along with the  
310 surrounding seismicity, has been described for subducted seamounts in Ecuador (Carnegie  
311 ridge; Leon-Rios et al., 2021) and Costa Rica (Husen et al., 2002). Finally, sections P7 and  
312 P8 show a large high ( $>1.80$ )  $V_p/V_s$  anomaly (labeled A8 in Figure 4) that extends for about  
313 100 km in the upper crust.

314

## 315 **5. Interpretation and Discussion**

### 316 *Seismic distribution and first-order structures*

317 Our derived 3D  $V_p$ ,  $V_s$  and  $V_p/V_s$  velocity models show the structure of the subducting  
318 Nazca plate down to 200 km depth (Figure 3 and 4). The upper continental crust has  
319 seismic velocities  $V_p \sim 5.0 - 7.0$  km/s and  $V_s \sim 3.0 - 4.0$  km/s. The continental Moho  
320 discontinuity associated with  $V_p \sim 7.7$  km/s implies a crustal thickness of the South  
321 American plate of around 40 – 50 km below the forearc, which is consistent with previous  
322 observations (e.g., Husen et al., 2000; Haberland et al., 2001). At a distance of 300 km east  
323 of the trench and at depths  $> \sim 50$  km, we observe the mantle wedge in most of the  
324 profiles (see Figure 3).

325 Below the coastal area, the seismicity shows several clusters that could be associated with  
326 regional structural features of the upper and lower plate. Southward from the Mejillones  
327 Peninsula (P4 to P8, Figure 3 and 4) the seismicity appears to be distributed in lineaments  
328 (L1, L2, L3) striking northwest, in concordance with structures observed onshore in the  
329 upper plate (Figure 1; Mavor et al. 2020, and references therein), while to the north the  
330 seismicity presents a more heterogenous distribution. This change could reflect a  
331 latitudinal segmentation of the active structures near the interplate boundary, at least  
332 when considering the coverage of our relocated catalog. In particular, P6 and P7 show  
333 dense clusters of seismicity offshore, which suggest the presence of west- and east-

334 vergent structures that could be influenced by the Taltal ridge subduction and/or the  
335 obliquity of the AFS in the area (Mavor et al. 2020).

336 At greater depths, we observe two prominent features in the seismicity distribution: (1)  
337 intense seismic activity at ~100 km depth that coincides with a low Vp/Vs region (labeled  
338 A3 in Figure 4) which collocates with the subducting Nazca plate (P1 to P3 in Figure 3). We  
339 note that previous studies have identified Vp/Vs ratios with similar values (Herrera et al.,  
340 2018). These reduced Vp/Vs values suggest a more rigid and dehydrated slab prone to a  
341 localized increase in intermediate-depth seismic activity. (2) We observe seismic activity at  
342 depths between 150 km – 200 km, located mostly at the northern profiles (sections P1-  
343 P4). P4 highlights the compressive Jujuy seismic nest (Valenzuela-Malebran et al., 2022).  
344 Compared with the Slab2 model (Hayes et al., 2018), our seismic catalog suggests a larger  
345 dip of the subducting Nazca plate at depths between 150 km - 200 km in the northern  
346 profiles (P1-P4).

#### 347 *Large-scale upper-crust features*

348 The continental crust shows a sequence of low and high Vp/Vs anomalies (Figure 3b).  
349 Along the coastal area, and correlating with the AFS, most of the profiles show high Vp/Vs  
350 values that could be associated with a more fractured crust due to this fracture zone. This  
351 correlation is particularly evident northward of ~25°S (Figure 4). In contrast, the coastal  
352 area in the zone of the Taltal ridge subduction is characterized by low Vp/Vs values which  
353 could be explained as a change in fluid transport inside the crust above this subducted  
354 feature. Coincidentally, the structures associated with the AFS show local rotations in this  
355 zone (Figure 4). In a similar way, at distances of ~200 km – 250 km from the trench (Figure  
356 3b), we observe another high Vp/Vs zone that coincides with the DFS. We infer that, in  
357 most profiles (Figure 3 and 4), this large-scale, seismically active geological structure  
358 extends down to ~50 km depth and is associated with the large porphyry copper deposits  
359 in the region (Reutter et al., 1996; Tomlinson and Blanco, 1997a; 1997b; Camus and  
360 Dilles, 2001). Eastward from the DFS, low Vp/Vs anomalies (A1-A4, <1.80; Figure 3 and 4)  
361 may be associated with an ancient magmatic arc that might have metamorphosed the

362 surrounding area (e.g. Diaz et al., 2012) and contributed to the accumulation of porphyry  
363 copper deposits (Comte et al., 2023; Chen and Wu, 2020). This observation coincides with  
364 the location of large copper mining operations in the area such as Chuquicamata, Gabriela  
365 Mistral and Escondida, and suggests that LET technique can be used as a tool to identify  
366 and characterize porphyry copper deposits at greater depths. In terms of absolute Vp  
367 velocity, and at crustal depths (< 50 km), the DFS is in general correlated with a transition  
368 from high Vp to the west to low Vp to the east of this structural limit, which could reflect a  
369 west-east thermal gradient related to active magmatic arc and subduction geometry  
370 (Contreras-Reyes et al., 2021) and/or the presence of high density basement units related  
371 to ancient volcanic arcs westward from the DFS (Bascuñán et al., 2016). The presence of  
372 cold and dense basement westward from the DFS is concordant with the more rigid (low  
373 Vp/Vs) crust observed between the AFS and DFS (Figures 3 and 4). East of the DFS, Vp/Vs  
374 values show a more heterogeneous distribution with higher strength (low Vp/Vs) in the  
375 southern portion of the Salar de Atacama basin (SdA) and to the southeast of the Salar de  
376 Punta Negra basin (Figure 4). By contrast, higher Vp/Vs anomalies are located to the north  
377 of the SdA. This heterogeneous distribution in strength could be related to the variability  
378 of the ancient basements in this region (e.g. Niemeyer et al., 2018) and the presence of  
379 regional structures, as the northwest Calama-Olacapato-El Toro lineament (COT, Lindsay  
380 et al., 2001) that seems to control the strength change between the northern and  
381 southern portions of the SdA region (figure 4).

382 At a regional scale, the succession of different strength bands (roughly north-south) in the  
383 forearc correlates well with large scale electric resistivity anomalies observed in  
384 magnetotellurics studies of the zone (Slezak et al., 2021; Contreras-Reyes et al., 2021),  
385 where crustal low strength anomalies (high Vp/Vs) correlate with low resistivity zones  
386 associated with costal large-scale structures (the AFS) and the DFS.

387

388 *Subducted slab, Mantle wedge and Fluid circulation*

389 First-order observations (sections P3-P7 in Figure 3) suggest a hydrated slab subducting  
390 down to ~80 - 90 km depth. At that point, we observe a transition to lower Vp/Vs (<1.76)  
391 suggesting a dehydration process consistent with temperature and pressure at these  
392 depths (Haberland and Rietbrock, 2001) which leads to a dryer slab at greater depths  
393 (>100 km). As mentioned before, the Vp/Vs model (Figure 3 and 4) shows elevated ratios  
394 (>1.77) at shallower depths (5 -10 km) that can be associated with the SdA and Salar Punta  
395 Negra basins. Moreover, the high Vp/Vs ratios allow us to estimate the in-depth extent of  
396 the fluids circulating down to ~30 km depth. At 30 km depth, we observe a predominantly  
397 low Vp/Vs region (<1.77) that covers most of the area of study. However, in profiles P7-P8  
398 a high Vp/Vs anomaly (labeled A8 in Figure 4) can be observed. This feature is more  
399 prominent at greater depths (~50 km), where we clearly observe a transition to higher  
400 values of Vp/Vs (>1.80). We attribute this anomaly to an increase in the fluid circulation  
401 promoted by the Taltal ridge, which subducts between 24°S – 25°S. The presence of large-  
402 scale, shallow oceanic features can cause basal erosion and fractures in the overriding  
403 plate (Scholz and Small, 1997; Contreras-Reyes et al., 2011) enhancing the transport of  
404 fluids from deeper to shallower depths (Collot et al., 2004; Marcaillou et al., 2016; Leon-  
405 Rios et al., 2021)

406 Finally, profiles P4 and P5 (Figure 3) show an elongated anomaly (labeled A6) with  
407 Vp/Vs~1.79 - 1.80 located at 50 km depth and ~ 300 km from the trench. We interpret this  
408 feature as fluids moving upwards from the plate interface towards the surface, promoting  
409 partial melting and feeding the northern edge of the LMB and other volcanic complexes  
410 (Haberland and Rietbrock, 2001; Diaz et al., 2006; 2012; Araya, 2019). The shallow  
411 seismicity observed ~400 km from the trench corroborates the hypothesis of fluid  
412 circulation in the area. We note that the SdA area (around profile P3-P4, Figure 4)  
413 correlates well with a part of the mantle wedge (depth ≥ 50 km) characterized by high Vp  
414 (>8.0 km/s) and low Vp/Vs (<1.70) bounded by low Vp (~7.5 km/s) and high Vp/Vs (>1.80),  
415 which suggest a correlation between anomalies associated with high fluid content (and  
416 high temperatures) and the active volcanism in the area, including the local eastward  
417 migration of the volcanic arc around the SdA.

418

419 **Conclusion**

420 Data from ~23,000 earthquakes recorded by a large temporary deployment that operated  
421 in northern Chile for an 8-month period allowed us to characterize the seismotectonic  
422 structure of the Taltal segment in northern Chile. We applied LET to jointly derive 3D  
423 seismic velocity models for  $V_p$ ,  $V_s$  and  $V_p/V_s$  and earthquake locations. The seismicity  
424 occurs mostly along the slab interface but also within large-scale structures in the  
425 overriding plate. At greater depths, we observe a change in the dip of the slab that we  
426 suggest results from a strong slab-pull. Offshore, we observe clustered seismicity that we  
427 interpret as a splay fault that reaches the slab interface. This seismicity appears to be a  
428 consequence of the Taltal ridge subducting in the southern part of the region.

429 The  $V_p$  and  $V_s$  seismic velocity models illuminate first-order structures such as the oceanic  
430 plate and the South American upper-crust. The  $V_p/V_s$  model identifies regions which  
431 change from reduced ( $<1.77$ ) to elevated ( $>1.77$ ) ratios that we interpret as large-scale  
432 fault systems that penetrate down to the seismogenic zone. The oceanic slab also shows a  
433 transition from elevated ( $>1.80$ ) to reduced ( $<1.76$ )  $V_p/V_s$  suggesting a highly hydrated  
434 plate at seismogenic depths that dehydrates and evolves into a dryer and more rigid slab  
435 at greater depths. The latter might also contribute to explaining the high rate of intraplate  
436 seismicity observed at ~200 km depth.

437 Low  $V_p/V_s$  anomalies ( $<1.75$ ) at shallow depths ( $<20$  km) collocate with sites of large  
438 copper mining operations and suggests the use of LET to illuminate locations of porphyry  
439 copper deposits. High  $V_p/V_s$  anomalies ( $>1.80$ ) at ~50 km depth suggest circulation of  
440 fluids caused by the incoming Taltal ridge that erodes and fractures the southern edge of  
441 overriding plate. They also suggest the presence of partial melting associated with the  
442 Lazufre Magmatic Body and other small volcanic systems.

443

444

445

446

447

448

449

450

#### 451 **Acknowledgments**

452 The authors acknowledge the funding from Fondecyt Postdoctorado 2022, No 322099;  
453 NSF-China-ANID PI18003; PIA AFB220002. Alejandro Faundez and Gerardo Peña who  
454 assisted in the network deployment. Section profiles and map view figures were made  
455 using GMTv5 (Wessel et al., 2013) and colored following the guidelines for CVD  
456 accessibility by Cramer et al. (2020).

#### 457 **Data availability**

458 Temporary network details in FDSN database (Andreas Rietbrock, Diana Comte, & Sergio  
459 Leon-Rios (2020): Taltal temporary deployment. International Federation of Digital  
460 Seismograph Networks. Dataset/Seismic Network. <https://doi.org/10.7914/mc8r-ft72>).

461 Initial and final models as well as hypocenter catalog, arrival times are available in  
462 ZENODO with the DOI 10.5281/zenodo.8271327.

463

#### 464 **References**

- 465 1. Abe, K. (1979). Size of great earthquakes of 1837–1974 inferred from tsunami data.  
466 *Journal of Geophysical Research: Solid Earth*, 84(B4), 1561-1568.
- 467 2. Aki, K., & Lee, W. H. K. (1976). Determination of three-dimensional velocity anomalies  
468 under a seismic array using first P arrival times from local earthquakes: 1. A  
469 homogeneous initial model. *Journal of Geophysical research*, 81(23), 4381-4399.

- 470 3. Aki, K., Christoffersson, A., & Husebye, E. S. (1977). Determination of the three-  
471 dimensional seismic structure of the lithosphere. *Journal of Geophysical Research*,  
472 82(2), 277-296.
- 473 4. Angermann, D., Klotz, J., & Reigber, C. (1999). Space-geodetic estimation of the  
474 Nazca-South America Euler vector. *Earth and Planetary Science Letters*, 171(3), 329-  
475 334.
- 476 5. Arabasz Jr, W. J. (1971). Geological and geophysical studies of the Atacama fault zone  
477 in northern Chile. Doctoral dissertation, California Institute of Technology.
- 478 6. Arabasz, W. J. (1968). Geologic structure of the Taltal Area, Northern Chile, in relation  
479 to the earthquake of December 28, 1966. *Bulletin of the Seismological Society of*  
480 *America*, 58(3), 835-842.
- 481 7. Araya Vargas, J., Meqbel, N. M., Ritter, O., Brasse, H., Weckmann, U., Yáñez, G., &  
482 Godoy, B. (2019). Fluid distribution in the Central Andes subduction zone imaged with  
483 magnetotellurics. *Journal of Geophysical Research: Solid Earth*, 124(4), 4017-4034.
- 484 8. Barrientos, S. (2018). The seismic network of Chile. *Seismological Research Letters*,  
485 89(2A), 467-474.
- 486 9. Bascuñán, S., Arriagada, C., Le Roux, J., Deckart, K., 2016. Unraveling the Peruvian  
487 Phase of the Central Andes: Stratigraphy, sedimentology and geochronology of the  
488 Salar de Atacama Basin (22°30'-23°S), northern Chile. *Basin Res.* 28, 365–392.  
489 <https://doi.org/10.1111/bre.12114>
- 490 10. Beck, S., Barrientos, S., Kausel, E., & Reyes, M. (1998). Source characteristics of  
491 historic earthquakes along the central Chile subduction Askew et Alzone. *Journal of*  
492 *South American Earth Sciences*, 11(2), 115-129.
- 493 11. Béjar-Pizarro, M., Carrizo, D., Socquet, A., Armijo, R., Barrientos, S., Bondoux, F., ... &  
494 Vigny, C. (2010). Asperities and barriers on the seismogenic zone in North Chile: state-  
495 of-the-art after the 2007 M w 7.7 Tocopilla earthquake inferred by GPS and InSAR  
496 data. *Geophysical Journal International*, 183(1), 390-406.

- 497 12. Brocher, T. M. (2005). Empirical relations between elastic wavespeeds and density in  
498 the Earth's crust. *Bulletin of the seismological Society of America*, 95(6), 2081-2092.
- 499 13. Calle-Gardella, D., Comte, D., Farías, M., Roecker, S., & Rietbrock, A. (2021). Three-  
500 dimensional local earthquake tomography of pre-Cenozoic structures in the coastal  
501 margin of central Chile: Pichilemu fault system. *Journal of Seismology*, 25(2), 521-533.
- 502 14. Calvert, A., Sandvol, E., Seber, D., Barazangi, M., Roecker, S., Mourabit, T., ... & Jabour,  
503 N. (2000). Geodynamic evolution of the lithosphere and upper mantle beneath the  
504 Alboran region of the western Mediterranean: Constraints from travel time  
505 tomography. *Journal of Geophysical Research: Solid Earth*, 105(B5), 10871-10898.
- 506 15. Camus, F., & Dilles, J. H. (2001). A special issue devoted to porphyry copper deposits  
507 of northern Chile. *Economic Geology*, 96(2), 233-237.
- 508 16. Cembrano, J., González, G., Arancibia, G., Ahumada, I., Olivares, V., & Herrera, V.  
509 (2005). Fault zone development and strain partitioning in an extensional strike-slip  
510 duplex: A case study from the Mesozoic Atacama fault system, Northern Chile.  
511 *Tectonophysics*, 400(1-4), 105-125.
- 512 17. Chen, H., & Wu, C. (2020). Metallogenesis and major challenges of porphyry copper  
513 systems above subduction zones. *Science China Earth Sciences*, 63, 899-918.
- 514 18. Chlieh, M., De Chabalier, J. B., Ruegg, J. C., Armijo, R., Dmowska, R., Campos, J., &  
515 Feigl, K. L. (2004). Crustal deformation and fault slip during the seismic cycle in the  
516 North Chile subduction zone, from GPS and InSAR observations. *Geophysical Journal  
517 International*, 158(2), 695-711.
- 518 19. Christensen, N. I. (1996). Poisson's ratio and crustal seismology. *Journal of  
519 Geophysical Research: Solid Earth*, 101(B2), 3139-3156.
- 520 20. Collot, J. Y., Marcaillou, B., Sage, F., Michaud, F., Agudelo, W., Charvis, P., ... & Spence,  
521 G. (2004). Are rupture zone limits of great subduction earthquakes controlled by  
522 upper plate structures? Evidence from multichannel seismic reflection data acquired

- 523 across the northern Ecuador–southwest Colombia margin. *Journal of Geophysical*  
524 *Research: Solid Earth*, 109(B11).
- 525 21. Comte, D., & Pardo, M. (1991). Reappraisal of great historical earthquakes in the  
526 northern Chile and southern Peru seismic gaps. *Natural hazards*, 4(1), 23-44.
- 527 22. Comte, D., Carrizo, D., Roecker, S., Ortega-Culaciati, F., & Peyrat, S. (2016). Three-  
528 dimensional elastic wave speeds in the northern Chile subduction zone: variations in  
529 hydration in the supraslab mantle. *Geophysical Supplements to the Monthly Notices*  
530 *of the Royal Astronomical Society*, 207(2), 1080-1105.
- 531 23. Comte, D., Farías, M., Calle-Gardella, D., Navarro-Aranguiz, A., Roecker, S., &  
532 Rietbrock, A. (2023). Anomalous intraslab structure revealed by the analysis of  
533 aftershocks of the Mw 6.7 Coquimbo-La Serena earthquake of 20 January 2019.  
534 *Tectonophysics*, 846, 229660.
- 535 24. Comte, D., Farias, M., Roecker, S., & Russo, R. (2019). The nature of the subduction  
536 wedge in an erosive margin: Insights from the analysis of aftershocks of the 2015 Mw  
537 8.3 Illapel earthquake beneath the Chilean Coastal Range. *Earth and Planetary Science*  
538 *Letters*, 520, 50-62.
- 539 25. Comte, D., Haessler, H., Dorbath, L., Pardo, M., Monfret, T., Lavenu, A., ... & Hello, Y.  
540 (2002). Seismicity and stress distribution in the Copiapo, northern Chile subduction  
541 zone using combined on-and off-shore seismic observations. *Physics of the earth and*  
542 *planetary interiors*, 132(1-3), 197-217.
- 543 26. Comte, D., Palma, G., Vargas, J. *et al.* Imaging the subsurface architecture in porphyry  
544 copper deposits using local earthquake tomography. *Sci Rep* **13**, 6812 (2023).  
545 <https://doi.org/10.1038/s41598-023-33820-w>
- 546 27. Contreras-Reyes, E., & Carrizo, D. (2011). Control of high oceanic features and  
547 subduction channel on earthquake ruptures along the Chile–Peru subduction zone.  
548 *Physics of the Earth and Planetary Interiors*, 186(1-2), 49-58.

- 549 28. Cooke, D. R., Hollings, P., & Walshe, J. L. (2005). Giant porphyry deposits:  
550 characteristics, distribution, and tectonic controls. *Economic geology*, 100(5), 801-  
551 818.
- 552 29. Cramer, F., Shephard, G. E., & Heron, P. J. (2020). The misuse of colour in science  
553 communication. *Nature communications*, 11(1), 1-10.
- 554 30. de Ballore, F. D. M. (1913, January). Historia sísmica de los andes meridionales al sur  
555 del paralelo XVI. In *Anales de la Universidad de Chile* (No. 71, pp. 87-129).
- 556 31. Delouis, B., Pardo, M., Legrand, D., & Monfret, T. (2009). The M<sub>w</sub> 7.7 Tocopilla  
557 earthquake of 14 November 2007 at the southern edge of the northern Chile seismic  
558 gap: Rupture in the deep part of the coupled plate interface. *Bulletin of the*  
559 *Seismological Society of America*, 99(1), 87-94.
- 560 32. Delph, J. R., Ward, K. M., Zandt, G., Ducea, M. N., & Beck, S. L. (2017). Imaging a  
561 magma plumbing system from MASH zone to magma reservoir. *Earth and Planetary*  
562 *Science Letters*, 457, 313-324.
- 563 33. DeMets, C., Gordon, R. G., Argus, D. F., & Stein, S. (1990). Current plate motions.  
564 *Geophysical journal international*, 101(2), 425-478.
- 565 34. DeMets, C., Gordon, R. G., Argus, D. F., & Stein, S. (1994). Effect of recent revisions to  
566 the geomagnetic reversal time scale on estimates of current plate motions.  
567 *Geophysical research letters*, 21(20), 2191-2194.
- 568 35. Deschamps, A., H. Lyon-Caen, and R. Madariaga (1980). Etude du tremblement de  
569 terre de Taltal (Chili 1966) à partir des ondes sismiques de longue période. *Ann.*  
570 *Geophys*, 36(2),
- 571 36. Díaz, D., Brasse, H., & Ticona, F. (2012). Conductivity distribution beneath Lascar  
572 volcano (Northern Chile) and the Puna, inferred from magnetotelluric data. *Journal of*  
573 *Volcanology and Geothermal Research*, 217, 21-29.
- 574 37. GeoForschungsZentrum, D. (2006). IPOC Seismic Network.

- 575 38. González-Vidal, D., Moreno, M., Sippl, C., Baez, J. C., Ortega-Culaciati, F. H., Lange, D.,  
576 ... & Araya, R. (2023). Relation between oceanic plate structure, patterns of interplate  
577 locking and microseismicity in the 1922 Atacama Seismic Gap. *Authorea Preprints*.
- 578 39. Götze, H. J., & Krause, S. (2002). The Central Andean gravity high, a relic of an old  
579 subduction complex?. *Journal of South American Earth Sciences*, 14(8), 799-811.
- 580 40. Götze, H. J., Lahmeyer, B., Schmidt, S., Strunk, S., & Araneda, M. (1990). Central Andes  
581 gravity data base. *Eos, Transactions American Geophysical Union*, 71(16), 401-407.
- 582 41. Greenfield, T., White, R. S., & Roecker, S. (2016). The magmatic plumbing system of  
583 the Askja central volcano, Iceland, as imaged by seismic tomography. *Journal of*  
584 *Geophysical Research: Solid Earth*, 121(10), 7211-7229.
- 585 42. Haberland, C., & Rietbrock, A. (2001). Attenuation tomography in the western central  
586 Andes: A detailed insight into the structure of a magmatic arc. *Journal of Geophysical*  
587 *Research: Solid Earth*, 106(B6), 11151-11167.
- 588 43. Hacker, B. R., Abers, G. A., & Peacock, S. M. (2003a). Subduction factory 1. Theoretical  
589 mineralogy, densities, seismic wave speeds, and H<sub>2</sub>O contents. *Journal of Geophysical*  
590 *Research: Solid Earth*, 108(B1).
- 591 44. Hacker, B. R., Peacock, S. M., Abers, G. A., & Holloway, S. D. (2003b). Subduction  
592 factory 2. Are intermediate-depth earthquakes in subducting slabs linked to  
593 metamorphic dehydration reactions?. *Journal of Geophysical Research: Solid Earth*,  
594 108(B1).
- 595 45. Hayes, G. P., Moore, G. L., Portner, D. E., Hearne, M., Flamme, H., Furtney, M., &  
596 Smoczyk, G. M. (2018). Slab2, a comprehensive subduction zone geometry model.  
597 *Science*, 362(6410), 58-61.
- 598 46. Herrera, C., Pastén-Araya, F., Cabrera, L., Potin, B., Rivera, E., Ruiz, S., ... & Contreras-  
599 Reyes, E. (2023). Rupture properties of the 2020 M<sub>w</sub> 6.8 Calama (northern Chile)  
600 intraslab earthquake. Comparison with similar intraslab events in the region.  
601 *Geophysical Journal International*, 232(3), 2070-2079.

- 602 47. Hicks, S. P., Rietbrock, A., Ryder, I. M., Lee, C. S., & Miller, M. (2014). Anatomy of a  
603 megathrust: The 2010 M8.8 Maule, Chile earthquake rupture zone imaged using  
604 seismic tomography. *Earth and Planetary Science Letters*, 405, 142-155.
- 605 48. Holtkamp, S. G., Pritchard, M. E., & Lohman, R. B. (2011). Earthquake swarms in South  
606 America. *Geophysical Journal International*, 187(1), 128-146.
- 607 49. Husen, S., Kissling, E., & Flueh, E. R. (2000). Local earthquake tomography of shallow  
608 subduction in north Chile: A combined onshore and offshore study. *Journal of*  
609 *Geophysical Research: Solid Earth*, 105(B12), 28183-28198.
- 610 50. Husen, S., Kissling, E., & Quintero, R. (2002). Tomographic evidence for a subducted  
611 seamount beneath the Gulf of Nicoya, Costa Rica: The cause of the 1990 Mw= 7.0 Gulf  
612 of Nicoya earthquake. *Geophysical Research Letters*, 29(8), 79-1.
- 613 51. Kanamori, H., Rivera, L., Ye, L., Lay, T., Murotani, S., & Tsumura, K. (2019). New  
614 constraints on the 1922 Atacama, Chile, earthquake from historical seismograms.  
615 *Geophysical Journal International*, 219(1), 645-661.
- 616 52. Kato, A., & Nakagawa, S. (2014). Multiple slow-slip events during a foreshock  
617 sequence of the 2014 Iquique, Chile Mw 8.1 earthquake. *Geophysical Research*  
618 *Letters*, 41(15), 5420-5427.
- 619 53. Kausel, E., & Campos, J. (1992). The Ms= 8 tensional earthquake of 9 December 1950  
620 of northern Chile and its relation to the seismic potential of the region. *Physics of the*  
621 *earth and planetary interiors*, 72(3-4), 220-235.
- 622 54. Kelleher, J. A. (1972). Rupture zones of large South American earthquakes and some  
623 predictions. *Journal of Geophysical Research*, 77(11), 2087-2103.
- 624 55. Kisslinger, C., & Engdahl, E. R. (1973). The interpretation of the Wadati diagram with  
625 relaxed assumptions. *Bulletin of the Seismological Society of America*, 63(5), 1723-  
626 1736.

- 627 56. Klein, E., Metois, M., Meneses, G., Vigny, C., & Delorme, A. (2018). Bridging the gap  
628 between North and Central Chile: insight from new GPS data on coupling complexities  
629 and the Andean sliver motion. *Geophysical Journal International*, 213(3), 1924-1933.
- 630 57. Köther, N., Götze, H. J., Gutknecht, B. D., Jahr, T., Jentzsch, G., Lücke, O. H., ... &  
631 Zeumann, S. (2012). The seismically active Andean and Central American margins: Can  
632 satellite gravity map lithospheric structures?. *Journal of Geodynamics*, 59, 207-218.
- 633 58. Kühn, C., Brasse, H., & Schwarz, G. (2018). Three-dimensional electrical resistivity  
634 image of the volcanic arc in Northern Chile—an appraisal of early magnetotelluric  
635 data. *Pure and Applied Geophysics*, 175(6), 2153-2165.
- 636 59. Kushnir, A. F., Lapshin, V. M., Pinsky, V. I., & Fyen, J. (1990). Statistically optimal event  
637 detection using small array data. *Bulletin of the seismological society of america*,  
638 80(6B), 1934-1950.
- 639 60. Legrand, D., Delouis, B., Dorbath, L., David, C., Campos, J., Marquez, L., ... & Comte, D.  
640 (2007). Source parameters of the Mw= 6.3 Aroma crustal earthquake of July 24, 2001  
641 (northern Chile), and its aftershock sequence. *Journal of south American earth  
642 sciences*, 24(1), 58-68.
- 643 61. León-Ríos, S., Bie, L., Agurto-Detzel, H., Rietbrock, A., Galve, A., Alvarado, A., ... &  
644 Woollam, J. (2021). 3D local earthquake tomography of the Ecuadorian margin in the  
645 source area of the 2016 Mw 7.8 Pedernales earthquake. *Journal of Geophysical  
646 Research: Solid Earth*, 126(3), e2020JB020701.
- 647 62. Lindsay, J. M., de Silva, S., Trumbull, R., Emmermann, R., & Wemmer, K. (2001). La  
648 Pacana caldera, N. Chile: a re-evaluation of the stratigraphy and volcanology of one of  
649 the world's largest resurgent calderas. *Journal of Volcanology and Geothermal  
650 Research*, 106(1), 145–173. [https://doi.org/https://doi.org/10.1016/S0377-  
651 0273\(00\)00270-5](https://doi.org/https://doi.org/10.1016/S0377-0273(00)00270-5)
- 652 63. Maksymowicz, A. (2015). The geometry of the Chilean continental wedge: Tectonic  
653 segmentation of subduction processes off Chile. *Tectonophysics*, 659, 183-196.

- 654 64. Marcaillou, B., Collot, J. Y., Ribodetti, A., d'Acremont, E., Mahamat, A. A., & Alvarado,  
655 A. (2016). Seamount subduction at the North-Ecuadorian convergent margin: Effects  
656 on structures, inter-seismic coupling and seismogenesis. *Earth and Planetary Science  
657 Letters*, 433, 146-158.
- 658 65. Mavor, S. P., Singleton, J. S., Gomila, R., Heuser, G., Seymour, N. M., Williams, S. A., ...  
659 & Stockli, D. F. (2020). Timing, kinematics, and displacement of the Taltal fault system,  
660 northern Chile: Implications for the Cretaceous tectonic evolution of the Andean  
661 margin. *Tectonics*, 39(2), e2019TC005832.
- 662 66. Meng, L., Huang, H., Bürgmann, R., Ampuero, J. P., & Strader, A. (2015). Dual  
663 megathrust slip behaviors of the 2014 Iquique earthquake sequence. *Earth and  
664 Planetary Science Letters*, 411, 177-187.
- 665 67. Metois, M., Socquet, A., Vigny, C., Carrizo, D., Peyrat, S., Delorme, A., ... & Ortega, I.  
666 (2013). Revisiting the North Chile seismic gap segmentation using GPS-derived  
667 interseismic coupling. *Geophysical Journal International*, 194(3), 1283-1294.
- 668 68. Metois, M., Vigny, C., & Socquet, A. (2016). Interseismic coupling, megathrust  
669 earthquakes and seismic swarms along the Chilean subduction zone (38–18 S). *Pure  
670 and Applied Geophysics*, 173(5), 1431-1449.
- 671 69. Mitchell, M. A., White, R. S., Roecker, S., & Greenfield, T. (2013). Tomographic image  
672 of melt storage beneath Askja Volcano, Iceland using local microseismicity.  
673 *Geophysical Research Letters*, 40(19), 5040-5046.
- 674 70. Monfret, T., Dorbath, L., Caminade, J. P., Pardo, M., Comte, D., & Ponce, L. (1995). The  
675 July 30, Antofagasta earthquake: an “Hypocritical” seismic event. *EOS, Trans. Am.  
676 geophys. Un*, 76(46), 427.
- 677 71. Montessus de Ballore F (1912) Historia sísmica de los Andes meridionales al sur del  
678 paralelo XVI. Imprenta Cervantes, Santiago, pp 545–591. Delouis, B., Monfret, T.,  
679 Dorbath, L., Pardo, M., Rivera, L., Comte, D., ... & Cisternas, A. (1997). The Mw= 8.0

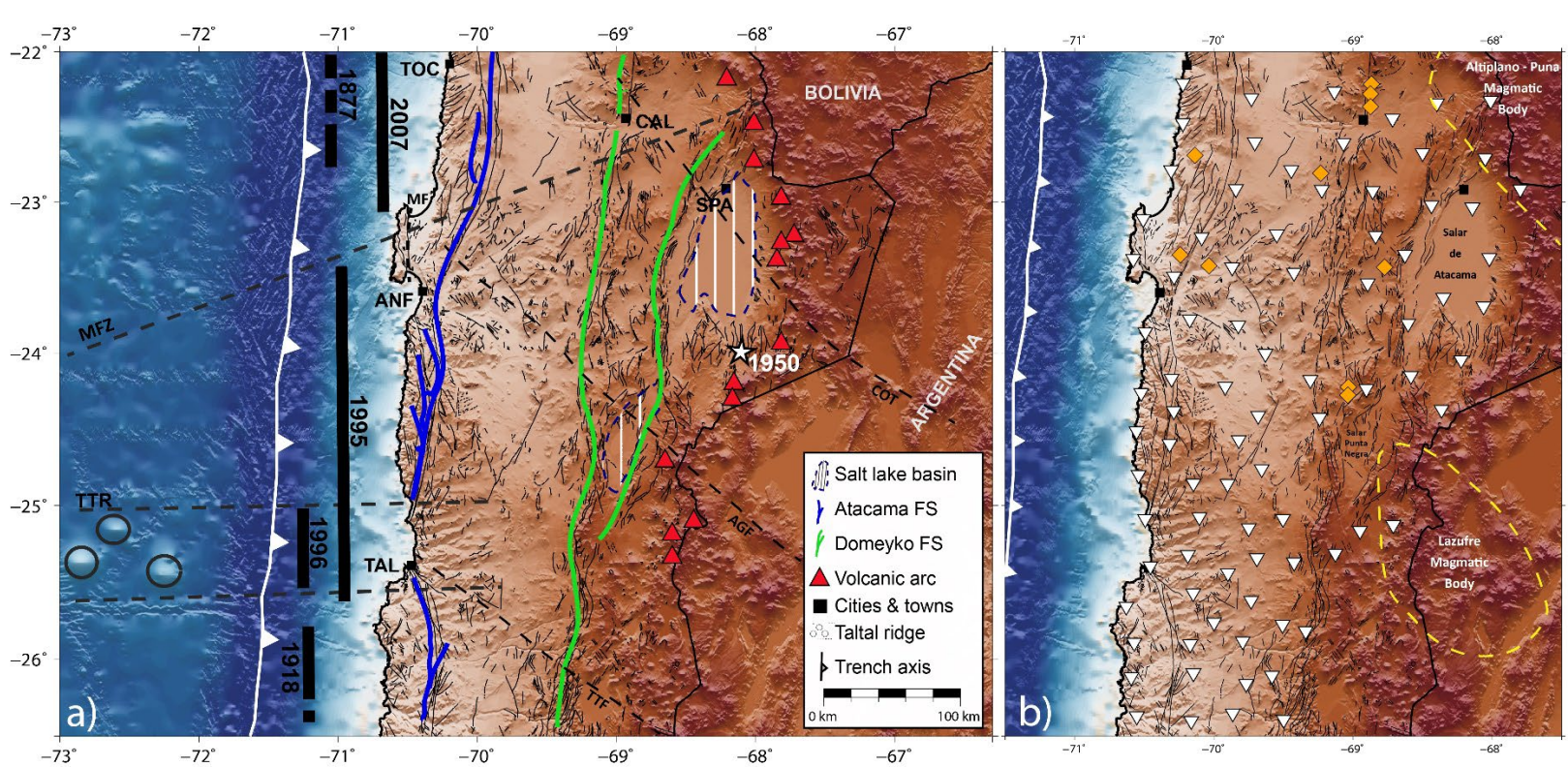
- 680 Antofagasta (northern Chile) earthquake of 30 July 1995: A precursor to the end of  
681 the large 1877 gap. *Bulletin of the Seismological Society of America*, 87(2), 427-445.
- 682 72. Niemeyer, H., Götze, J., Sanhueza, M., & Portilla, C. (2018). The Ordovician magmatic  
683 arc in the northern Chile-Argentina Andes between 21° and 26° south latitude. *Journal*  
684 *of South American Earth Sciences*, 81, 204–214.  
685 <https://doi.org/https://doi.org/10.1016/j.jsames.2017.11.016>
- 686 73. Norabuena, E. O., Dixon, T. H., Stein, S., & Harrison, C. G. (1999). Decelerating Nazca-  
687 South America and Nazca-Pacific plate motions. *Geophysical Research Letters*, 26(22),  
688 3405-3408.
- 689 74. Palacios, C., Ramírez, L. E., Townley, B., Solari, M., & Guerra, N. (2007). The role of the  
690 Antofagasta–Calama Lineament in ore deposit deformation in the Andes of northern  
691 Chile. *Mineralium Deposita*, 42(3), 301-308.
- 692 75. Pastén-Araya, F., Potin, B., Ruiz, S., Zerbst, L., Aden-Antoniów, F., Azúa, K., ... &  
693 Fuenzalida, A. (2021). Seismicity in the upper plate of the Northern Chilean offshore  
694 forearc: Evidence of splay fault south of the Mejillones Peninsula. *Tectonophysics*,  
695 800, 228706.
- 696 76. Peyrat, S., Madariaga, R., Buforn, E., Campos, J., Asch, G., & Vilotte, J. P. (2010).  
697 Kinematic rupture process of the 2007 Tocopilla earthquake and its main aftershocks  
698 from teleseismic and strong-motion data. *Geophysical Journal International*, 182(3),  
699 1411-1430.
- 700 77. Pisarenko, V. F., Kushnir, A. F., & Savin, I. V. (1987). Statistical adaptive algorithms for  
701 estimation of onset moments of seismic phases. *Physics of the earth and planetary*  
702 *interiors*, 47, 4-10.
- 703 78. Prévot, R., Roecker, S. W., Isacks, B. L., & Chatelain, J. L. (1991). Mapping of low P  
704 wave velocity structures in the subducting plate of the central New Hebrides,  
705 southwest Pacific. *Journal of Geophysical Research: Solid Earth*, 96(B12), 19825-  
706 19842.

- 707 79. Pritchard, M. E., De Silva, S. L., Michelfelder, G., Zandt, G., McNutt, S. R., Gottsmann,  
708 J., ... & Ward, K. M. (2018). Synthesis: PLUTONS: Investigating the relationship  
709 between pluton growth and volcanism in the Central Andes. *Geosphere*, 14(3), 954-  
710 982.
- 711 80. Rawles, C., & Thurber, C. (2015). A non-parametric method for automatic  
712 determination of P-wave and S-wave arrival times: application to local micro  
713 earthquakes. *Geophysical Journal International*, 202(2), 1164-1179.
- 714 81. Reutter, K. J., Scheuber, E., & Chong, G. (1996). The Precordilleran fault system of  
715 Chuquicamata, northern Chile: Evidence for reversals along arc-parallel strike-slip  
716 faults. *Tectonophysics*, 259(1-3), 213-228.
- 717 82. Reutter, K. J., Scheuber, E., & Helmcke, D. (1991). Structural evidence of orogen-  
718 parallel strike slip displacements in the Precordillera of northern Chile. *Geologische*  
719 *Rundschau*, 80(1), 135-153.
- 720 83. Richards, J. (2016). Clues to hidden copper deposits. *Nature Geoscience*, 9(3), 195-  
721 196.
- 722 84. Riller, U., Götze, H. J., Schmidt, S., Trumbull, R. B., Hongn, F., & Petrinovic, I. A. (2006).  
723 Upper-crustal structure of the Central Andes inferred from dip curvature analysis of  
724 isostatic residual gravity. In *The Andes* (pp. 327-336). Springer, Berlin, Heidelberg.
- 725 85. Roecker, S., Thurber, C., & McPhee, D. (2004). Joint inversion of gravity and arrival  
726 time data from Parkfield: New constraints on structure and hypocenter locations near  
727 the SAFOD drill site. *Geophysical Research Letters*, 31(12).
- 728 86. Roecker, S., Thurber, C., Roberts, K., & Powell, L. (2006). Refining the image of the San  
729 Andreas Fault near Parkfield, California using a finite difference travel time  
730 computation technique. *Tectonophysics*, 426(1-2), 189-205.
- 731 87. Ruegg, J. C., Campos, J., Armijo, R., Barrientos, S., Briole, P., Thiele, R., ... & Serrurier,  
732 L. (1996). The Mw= 8.1 Antofagasta (North Chile) earthquake of July 30, 1995: first

- 733 results from teleseismic and geodetic data. *Geophysical Research Letters*, 23(9), 917-  
734 920.
- 735 88. Ruiz, S., & Madariaga, R. (2018). Historical and recent large megathrust earthquakes  
736 in Chile. *Tectonophysics*, 733, 37-56.
- 737 89. Ruiz, S., Metois, M., Fuenzalida, A., Ruiz, J., Leyton, F., Grandin, R., ... & Campos, J.  
738 (2014). Intense foreshocks and a slow slip event preceded the 2014 Iquique Mw 8.1  
739 earthquake. *Science*, 345(6201), 1165-1169.
- 740 90. Salazar, D., Easton, G., Goff, J., Guendon, J. L., González-Alfaro, J., Andrade, P., ... &  
741 Campos, J. (2022). Did a 3800-year-old  $M_w \sim 9.5$  earthquake trigger major social  
742 disruption in the Atacama Desert?. *Science advances*, 8(14), eabm2996.
- 743 91. Scheuber, E., & Gonzalez, G. (1999). Tectonics of the Jurassic-Early Cretaceous  
744 magmatic arc of the north Chilean Coastal Cordillera (22–26 S): A story of crustal  
745 deformation along a convergent plate boundary. *Tectonics*, 18(5), 895-910.
- 746 92. Scholz, C. H., & Small, C. (1997). The effect of seamount subduction on seismic  
747 coupling. *Geology*, 25(6), 487-490.
- 748 93. Schurr, B., & Rietbrock, A. (2004). Deep seismic structure of the Atacama basin,  
749 northern Chile. *Geophysical Research Letters*, 31(12).
- 750 94. Schurr, B., Rietbrock, A., Asch, G., Kind, R., & Oncken, O. (2006). Evidence for  
751 lithospheric detachment in the central Andes from local earthquake tomography.  
752 *Tectonophysics*, 415(1-4), 203-223.
- 753 95. Sella, G. F., Dixon, T. H., & Mao, A. (2002). REVEL: A model for recent plate velocities  
754 from space geodesy. *Journal of Geophysical Research: Solid Earth*, 107(B4), ETG-11.
- 755 96. Sippl, C., Schurr, B., Asch, G., & Kummerow, J. (2018). Seismicity structure of the  
756 northern Chile forearc from > 100,000 double-difference relocated hypocenters.  
757 *Journal of Geophysical Research: Solid Earth*, 123(5), 4063-4087.

- 758 97. Sippl, C., Schurr, B., Münchmeyer, J., Barrientos, S., & Oncken, O. (2023). The  
759 Northern Chile forearc constrained by 15 years of permanent seismic monitoring.  
760 *Journal of South American Earth Sciences*, 104326.
- 761 98. Ślęzak, K., Díaz, D., Vargas, J. A., Cordell, D., Reyes-Cordova, F., & Segovia, M. J.  
762 (2021). Magnetotelluric image of the Chilean subduction zone in the Salar de Atacama  
763 region (23°-24° S): Insights into factors controlling the distribution of volcanic arc  
764 magmatism. *Physics of the Earth and Planetary Interiors*, 318, 106765.
- 765 99. Spakman, W., & Nolet, G. (1988). Imaging algorithms, accuracy and resolution in delay  
766 time tomography. *Mathematical geophysics: A survey of recent developments in*  
767 *seismology and geodynamics*, 155-187.
- 768 100. Tomlinson, A. J., & Blanco, N. (1997a). Structural evolution and displacement history  
769 of the west fault systems, Precordillera, Chile, part 1, Post-mineral history, paper  
770 presented at VIII Congreso Geológico Chileno. *Soc. Geol. de Chile, Antofagasta, Chile*.
- 771 101. Tomlinson, A. J., & Blanco, N. (1997b). Structural evolution and displacement history  
772 of the west fault systems, Precordillera, Chile, part 2, Post-mineral history, paper  
773 presented at VIII Congreso Geológico Chileno. *Soc. Geol. de Chile, Antofagasta, Chile*.
- 774 102. Valenzuela-Malebrán, C., Cesca, S., López-Comino, J. A., Zeckra, M., Krüger, F., &  
775 Dahm, T. (2022). Source mechanisms and rupture processes of the Jujuy seismic nest,  
776 Chile-Argentina border. *Journal of South American Earth Sciences*, 117, 103887.
- 777 103. Victor, P., Oncken, O., & Glodny, J. (2004). Uplift of the western Altiplano plateau:  
778 Evidence from the Precordillera between 20 and 21 S (northern Chile). *Tectonics*,  
779 23(4).
- 780 104. Victor, P., Sobiesiak, M., Glodny, J., Nielsen, S. N., & Oncken, O. (2011). Long-term  
781 persistence of subduction earthquake segment boundaries: Evidence from Mejillones  
782 Peninsula, northern Chile. *Journal of Geophysical Research: Solid Earth*, 116(B2).

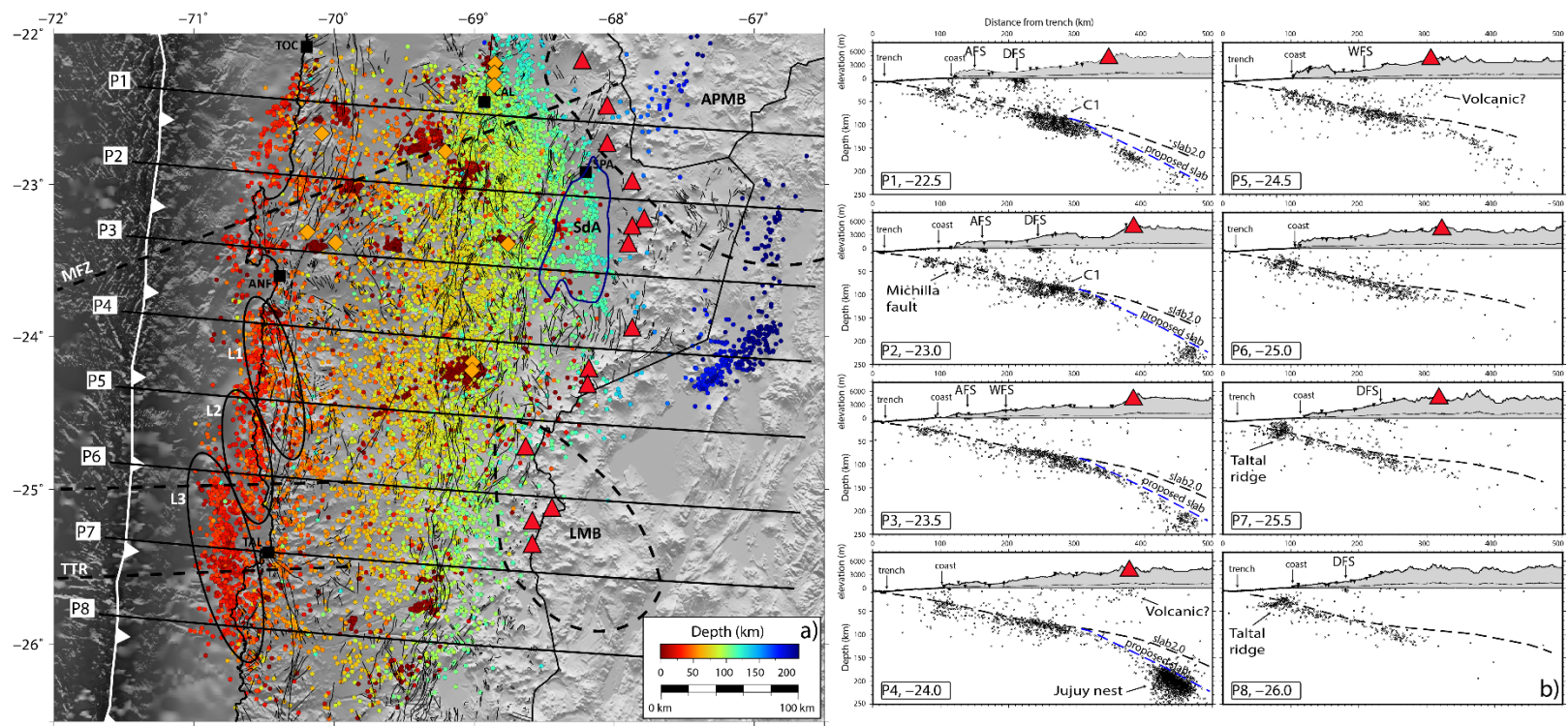
- 783 105. Von Huene, R., Corvalán, J., Flueh, E. R., Hinz, K., Korstgard, J., Ranero, C. R., &  
784 Weinrebe, W. (1997). Tectonic control of the subducting Juan Fernández Ridge on the  
785 Andean margin near Valparaíso, Chile. *Tectonics*, 16(3), 474-488.
- 786 106. Wadati, K., & Oki, S. (1933). On the travel time of earthquake waves. (Part II). *Journal*  
787 *of the Meteorological Society of Japan*. Ser. II, 11(1), 14-28. Ward, K. M., Delph, J. R.,  
788 Zandt, G., Beck, S. L., & Ducea, M. N. (2017). Magmatic evolution of a Cordilleran  
789 flare-up and its role in the creation of silicic crust. *Scientific reports*, 7(1), 1-8.
- 790 107. Ward, K. M., Delph, J. R., Zandt, G., Beck, S. L., & Ducea, M. N. (2017). Magmatic  
791 evolution of a Cordilleran flare-up and its role in the creation of silicic crust. *Scientific*  
792 *reports*, 7(1), 9047.
- 793 108. Ward, K. M., Zandt, G., Beck, S. L., Christensen, D. H., & McFarlin, H. (2014). Seismic  
794 imaging of the magmatic underpinnings beneath the Altiplano-Puna volcanic complex  
795 from the joint inversion of surface wave dispersion and receiver functions. *Earth and*  
796 *Planetary Science Letters*, 404, 43-53.
- 797 109. Wessel, P., W. H. F. Smith, R. Scharroo, J. Luis, and F. Wobbe, Generic Mapping Tools:  
798 Improved Version Released, *EOS Trans. AGU*, 94(45), p. 409–410, 2013.  
799 doi:10.1002/2013EO450001.
- 800 110. Willis, B. (1929). Earthquake conditions in Chile. Carnegie Institution of Washington,  
801 382, 178p.
- 802 111. Yáñez-Cuadra, V., Ortega-Culaciati, F., Moreno, M., Tassara, A., Krumm-Nualart, N.,  
803 Ruiz, J., ... & Benavente, R. (2022). Interplate coupling and seismic potential in the  
804 Atacama Seismic Gap (Chile): Dismissing a rigid Andean sliver. *Geophysical Research*  
805 *Letters*, 49(11), e2022GL098257.
- 806
- 807
- 808



812 Figure 1. **a)** Seismotectonic setting of the study area. Solid black lines represent the extent  
 813 of historical megathrust earthquakes in the area (Monfret et al., 1995; Ruegg et al., 1996;  
 814 Delouis et al., 1997; Delouis et al., 2009; Peyrat et al., 2010; Bejar-Pizarro et al., 2010; Ruiz  
 815 and Madariaga, 2018) and white star show the epicenter of the intraplate 1950 Calama  
 816 earthquake (Kausel and Campos, 1992). Solid blue and green lines mark the main trend of  
 817 the Atacama and Domeyko Fault Systems, respectively. Segmented black lines represent  
 818 crustal faults: COT, Calama-Olacapato-Toro; AGF, Achibarca-Galan fault ; TTF, Taltal fault;  
 819 MF, Mejillones fault. Red triangles show the active volcanoes and segmented lines offshore  
 820 indicate the projection of the Mejillones Fracture Zone (MFZ) and Taltal ridge (TTR). Black  
 821 squares highlight major settlements in the region, TOC: Tocopilla, CAL: Calama, SPA: San  
 822 Pedro de Atacama, ANF: Antofagasta, TAL: Taltal. **b)** Distribution of the temporary seismic  
 823 experiment with 88 short period 4.5 Hz geophones (white triangles) recording at 200 sps.  
 824 The network collected data for 8 months, between March and October 2020. Yellow  
 825 squares indicate major mining operations in the area. Black squares represent settlements  
 826 in the region.

827

828



837 Figure 2. Seismicity distribution for the Taltal segment. **a)** Map view with earthquakes as  
 838 small circles colored according to depth. Yellow squares indicate major mining operations  
 839 in the area. Red triangles represent the active volcanic arc. The ellipses show the Norwest  
 840 lineaments L1, L2, L3 described in text. Black squares show the main settlements. MFZ:  
 841 Mejillones Fracture Zone, TTR: Taltal Ridge, APMB: Altiplano-Puna Magmatic Body, LMB:  
 842 Lazufre Magmatic Body, SdA: Salar de Atacama. **b)** W-E profiles with the seismic distribution  
 843 in depth as shown in scale. Inverted triangles represent the station distribution in the area.  
 844 The volcanic arc is represented by red triangles. AFS: Atacama Fault System, DFS: Domeyko  
 845 Fault System.

846

847

848

849

850

851

852

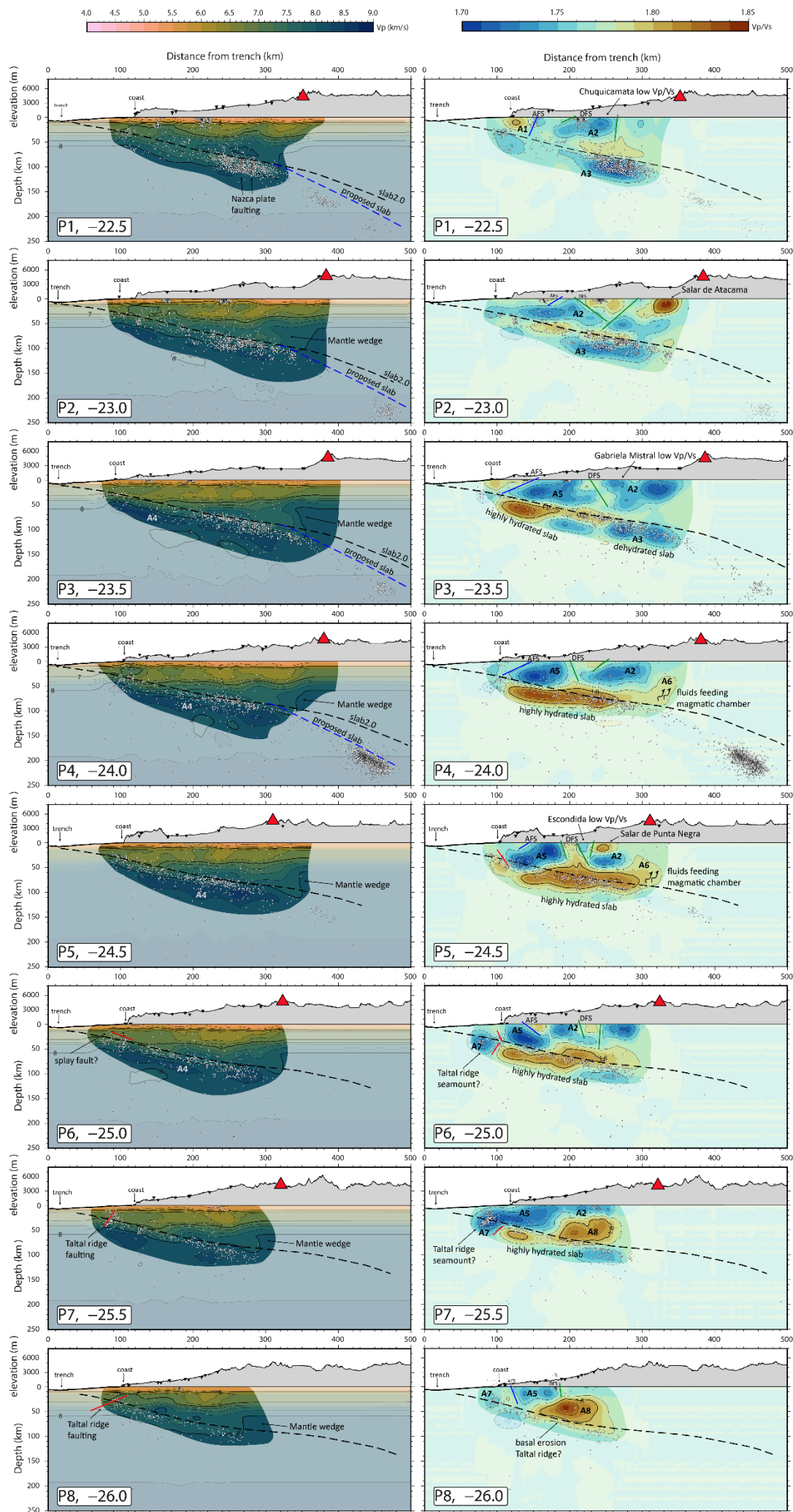


Figure 3. Cross sections of the 3D velocity model for  $V_p$  (left) and  $V_p/V_s$  (right). Results are shown along 8 W-E profiles shown in Figure 3.  $V_p$  velocities and  $V_p/V_s$  ratios are color-coded and isocontours are plotted every 0.25 km/s and 0.05 for  $V_p$  and  $V_p/V_s$ , respectively. Well-resolved areas are highlighted based on the resolution tests. Width for projection of hypocenters and stations is 20 km. Relocated hypocenters are plotted as white circles, and stations are represented by inverted triangles. Proposed slab interface (see text for further details) is represented by segmented blue line while slab 2.0 (Hayes et al., 2018) is shown with segmented black line. Red triangles indicate the position of the volcanic arc. AFS: Atacama Fault System, DFS: Domeyko Fault System; A1-A8, anomalies described in text.

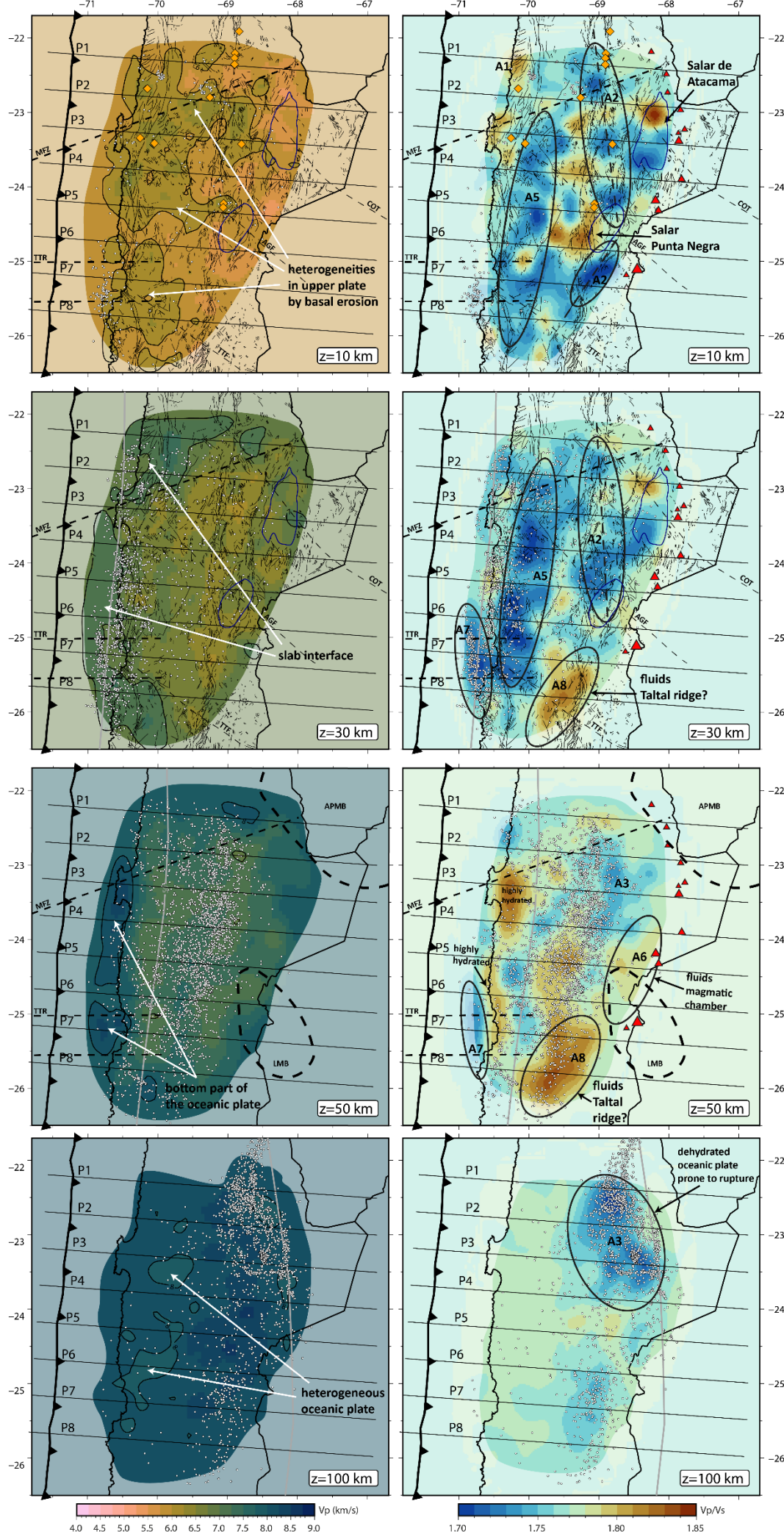


Figure 4. 3D velocity models,  $V_p$  (left) and  $V_p/V_s$  (right) shown in horizontal slices at 10, 30, 50 and 100 km depth. Well-resolved areas are highlighted based on the resolution tests. Red triangles indicate the position of the volcanic arc. Major mining operations are represented by yellow squares in the 10 km depth slices. Velocity anomalies collocated to surface observations and cities in the text are also shown in the 10 km depth slice. Location of cross section profiles of Figure 3 are shown as black solid lines. Corresponding slab depth contour (Hayes et al., 2018) is represented by a thick gray line. Seismicity is plotted by depth,  $d$ , with  $d \leq 10$  km in  $z = 10$  km,  $20 < d \leq 35$  km in  $z = 30$  km,  $40 < d \leq 55$  km in  $z = 50$  km, and  $90 < d \leq 110$  km in  $z = 100$  km. Fault map is plotted at shallower depths (10-30 km). MFZ: Mejillones Fracture Zone, TTR: Taltal Ridge, APMB: Altiplano-Puna Magmatic Body, LMB: Lazufre Magmatic Body. The anomalies labeled A1-A8, are described in the text.